Reducing inter-pixel crosstalk in HgCdTe detectors

Opt. Quant. Electron. manuscript No.
(will be inserted by the editor)

Reducing inter-pixel crosstalk in HgCdTe detectors

Marco Vallone · Michele Goano · Francesco Bertazzi · Giovanni Ghione · Andrea Palmieri · Stefan Hanna · Detlef Eich · Heinrich Figgemeier

January 10, 2020

Abstract In state-of-the-art, large format, HgCdTe-based infrared focal plane arrays the typical pixel size ($3-10\,\mu$m) is of the order of the operating wavelength and much smaller than the carrier diffusion length. This makes inter-pixel crosstalk a limiting factor, especially in planar structures. Employing three-dimensional electromagnetic and electrical simulations we show that, besides reducing the dark current through Auger suppression, majority carrier depletion of the detector absorber is also effective in curtailing the inter-pixel crosstalk due to carrier diffusion. In the case of a $5\,\mu$m-pitch pixel, a proper design of the absorber composition and doping profile allows to reduce inter-pixel crosstalk by more than a factor of two when increasing the reverse bias from -0.1 V to -0.5 V, keeping the contribution to crosstalk coming from carrier diffusion between 2% and 12% in the mid- and long-wavelength infrared spectrum.

Keywords HgCdTe · Infrared photodetectors · FDTD simulations · focal plane arrays · Multiphysics simulations

1 Introduction

The II-VI alloy HgCdTe is one of the most versatile materials for the realization of large format infrared (IR) two-dimensional focal plane arrays (FPAs) of pixels [1]. However, the small bandgap needed for IR operation often requires expensive and heavy cryogenic cooling systems to reduce the dark current [2,3]. According to the literature, High Operating Temperature (HOT) detectors [4–6], obtained e.g. with *n*B*n* structures [7–9] or with fully-depleted double-layer planar heterostructures (DLPH) [10], should ultimately lead to room-

Marco Vallone · Michele Goano · Francesco Bertazzi · Giovanni Ghione · Andrea Palmieri
Dipartimento di Elettronica e Telecomunicazioni, Politecnico di Torino, Corso Duca degli Abruzzi 24, 10129, Torino, Italy

Stefan Hanna · Detlef Eich · Heinrich Figgemeier
AIM Infrarot-Module GmbH, Theresienstraße 2, D-74072 Heilbronn, Germany

E-mail: marco.vallone@polito.it

temperature operation. In this context, carrier depletion of DLPH's absorber is effective in suppressing the Auger carrier generation in quasi-neutral regions, one of the largest sources of dark current in HgCdTe-based detectors [3, 10–12].

Large format IR-FPAs are employed as key components in advanced IR imaging systems conceived for civilian and military applications, and their spatial resolution greatly depends on the density of pixels per unit area [2, 13–19]. Since FPAs spatially sample the imaged scene, a critical reference value is the minimum useful pixel pitch P for diffraction-limited optical systems fulfilling the Nyquist criterion [19–22], estimated around $3\,\mu$m for the mid-wavelength IR band (MWIR, wavelength $\lambda \in [3,5]\,\mu$m) and around $5\,\mu$m for the long-wavelength IR band (LWIR, $\lambda \in [8,14]\,\mu$m). When such technologically challenging target values for P are considered, the inter-pixel crosstalk [16] can become a limiting factor, especially when planar structures are considered. With *inter-pixel crosstalk* we mean here the electrical response of an FPA pixel when an IR beam illuminates another pixel of the array, excluding any contribution from the read-out integrated circuit (ROIC). The present work describes, almost in form of tutorial, a possible modeling method suitable to study inter-pixel crosstalk, discussing the necessary computational steps and describing the effects of carrier depletion on a planar detector with $P = 5\,\mu$m. Besides determining a substantial reduction of the dark current, carrier depletion is shown to be effective also in reducing the diffusive inter-pixel crosstalk [22, 23], which is particularly relevant when P (5 – 15 μm in state-of-the-art devices) becomes much smaller than the diffusion length of minority carriers (in the order of tens of micrometers for LWIR detectors at typical operating temperatures [24]). Further investigations are under way to assess the effects of absorber doping, thickness and compositional gradient on the detector performance at different temperatures, and will be the object of a separate contribution.

In Section 2 we describe the detector structure, in Section 3 the modeling method is outlined, and in Section 4 the results are presented and discussed, showing the effects of reverse bias on the depletion of carriers and on the inter-pixel crosstalk coming from their lateral diffusion. In the end, in Section 5 the main results are summarized.

2 Photodetector structure

We considered a small modification of an epitaxial structure described in the literature [25], known to be able to cut down the dark current by suppressing Auger generation via majority carrier depletion. This choice is motivated by our intention to show that carrier depletion is also suitable to effectively decrease the diffusive inter-pixel crosstalk.

Fig. 1 shows the photodetector structure, with the definitions of the central pixel (CP), the neighboring (NN) and the corner-neighboring (CN) pixels: it is a planar 5×5 miniarray with $5\,\mu$m-wide square pixels whose doping scheme is p-on-n, without trenches (planar structure). Above a CdTe substrate, a wide-bandgap n-$Hg_{0.6}Cd_{0.4}Te$ layer was grown, doped with donor concentration $N_D = 5 \times 10^{17}$ cm^{-3}. It is followed by a 5 μm thick, low donor-doped, narrow-bandgap HgCdTe absorber layer ($N_D = 1 \times 10^{14}$ cm^{-3}), and by another wide-bandgap $Hg_{0.6}Cd_{0.4}Te$ layer, with the same low donor concentration. A p-n junction at a depth of $\approx 2.5\,\mu$m was defined by simulating an ion implantation, resulting in an error-function-shaped acceptor density N_A, ranging from 5×10^{16} cm^{-3} just below the bias contact to virtually zero at the given depth. The absorber layer was given a graded composition, varying the Cd mole fraction from $x = 0.25$ to $x = 0.19$, from its lower to its upper interface. In this way, the absorber compositional grading makes the detector suitable for both mid wavelength and long wavelength operation. In addition, the quasi-electric field en-

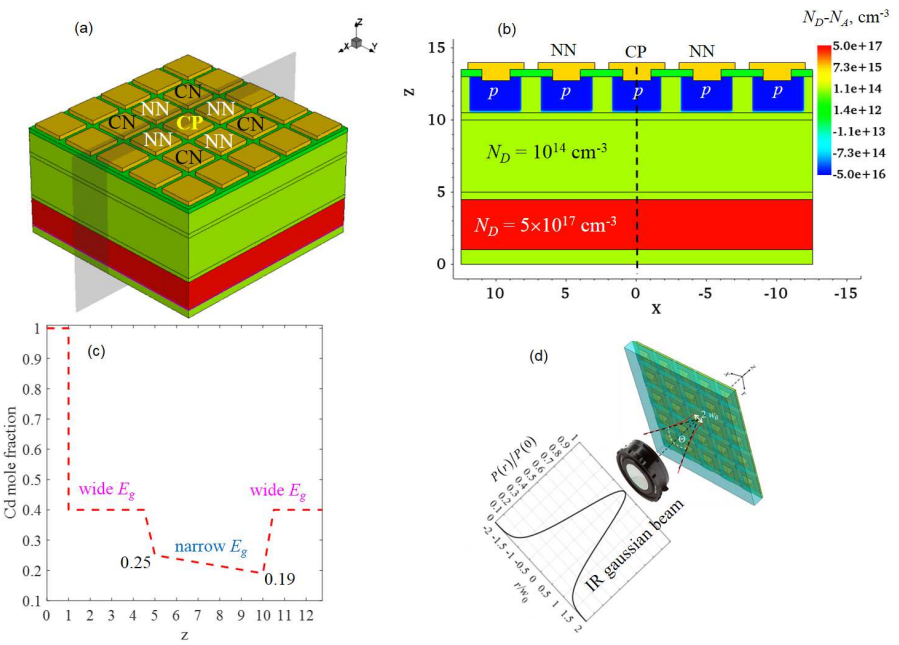

Fig. 1 (a) The 3D miniarray. CP, NN, and CN mark respectively the central pixel (CP), the neighboring (NN) and the corner-neighboring (CN) pixels. (b) The doping distribution shown in a two dimensional (2D) cutplane. (c) The Cd mole fraction x of $Hg_{1-x}Cd_xTe$ profile along a vertical z-cutline (E_g is the bandgap). (d) A sketch of the illumination, as a narrow Gaussian beam focused on the central pixel from below.

suing from the compositional grading contributes to sweep-out the photogenerated minority carriers (holes) from the low donor-doped absorber, before they diffuse laterally contributing to crosstalk [26,27]. The bias contacts were connected to the p-doped regions through a square metallic layer partly extending over a $0.3\,\mu$m thick CdTe passivation layer that covers the upper face of the FPA. The HgCdTe properties were described through the models reported in [22], taking into account the composition, doping, and temperature dependence of the HgCdTe alloy. The Shockley-Read-Hall (SRH) recombination processes were modeled as in [28] considering a lifetime around $100\,\mu$s, neglecting instead trap-assisted or band-to-band tunneling processes [29–31]. Fermi-Dirac statistics and incomplete dopant ionization were taken into account, with activation energies for HgCdTe alloys estimated according to [32,33].

Regarding the illumination, we considered a narrow Gaussian beam illuminating the array from below. The beam, with power flux $\Phi(r) = \Phi_0 \exp\left(-2r^2/w_0^2\right)$, is centered on the miniarray's CP and focused on the illuminated face, and the beam axis is orthogonal to the detector horizontal plane xy. Φ_0 is the optical power flux along the beam axis, r is the radial distance from the beam axis and w_0 is the beam waist radius, for which we chose $w_0 = 2.5\,\mu$m. It must be noticed that $\Phi(r)$ never goes to zero, hence the beam tail also illuminates partially the CP neighboring pixels.

3 Modeling method

The geometry, doping and composition profiles were defined employing the TCAD Sentaurus three-dimensional (3D) numerical simulator by Synopsys [34], also used to perform the electrical simulations in the drift-diffusion approximation.

3.1 Electromagnetic simulations

The first step consisted in obtaining the solution of the electromagnetic problem under monochromatic Gaussian beam illumination. Since the composition profiles of absorber and transition regions are not uniform, we sampled their profiles as described in [35], converting them to staircases of $N = 30$ sublayers with uniform complex refractive index $n_r + i\kappa$, evaluated according to the composition of each sublayer ([22], Table I) and for all the considered wavelengths $\lambda_n \in [2,12]\,\mu$m of the illuminating IR radiation. The λ interval was sampled considering a wavelength resolution of $0.5\,\mu$m for $\lambda_n \in [2,9]\,\mu$m, and $0.1\,\mu$m for $\lambda_n \geq 9\,\mu$m. A fine λ sampling is important especially around the cutoff wavelength, where internal reflections and interference effects generate a rich resonance-like phenomenology, that in turn depends on the absorber graded composition [22,35,36]. The computational box includes air layers located above and below the miniarray, and the optical boundary conditions (BC) along all the sides of the box are absorbing (this is obtained with convolutional perfectly matching layers [37]). With this approach, the Sentaurus Device Electromagnetic Wave Solver (EMW) [38], integrated in the Synopsys TCAD Sentaurus suite, was able to solve the electromagnetic problem by a full-wave approach, according to the Finite Differences Time Domain (FDTD) method and discretizing the miniarray into a Yee's grid of $\approx 3.4 \times 10^6$ elements [39,40].

The absorbed photon density A_{opt} (number of absorbed photons per unit volume and time) can be evaluated as the divergence of the time-averaged Poynting vector $\langle \mathbf{S} \rangle$ [41–44]

$$A_{\text{opt}}(\lambda_n) = -\frac{\nabla \cdot \langle \mathbf{S}(\lambda_n) \rangle}{hc/\lambda_n}, \tag{1}$$

constituting the solution of the electromagnetic problem (h is the Planck's constant, c is the light velocity in vacuum, and the material's complex refractive index is included in $\mathbf{S}$ through Maxwell's equations as shown e.g. in [22] Eqs. (8-10)). The optical generation rate distribution G_{opt} into the FPA due to interband optical absorption is given by $G_{\text{opt}}(\lambda_n) = \eta A_{\text{opt}}(\lambda_n)$, where the quantum yield η, defined as the fraction of absorbed photons which are converted to photogenerated electron-hole pairs, was assumed to be unitary.

3.2 Electrical simulations and figures of merit

The electrical problem was solved within the drift-diffusion approximation, as outlined e.g. in [45,22,46,47]. Electric contacts were treated as Ohmic with zero resistance, where charge neutrality and equilibrium were assumed. Ideal Neumann BCs were applied to the outer boundaries of the array, and the drift-diffusion equations were solved by the Finite Box (FB) method, setting $T = 140$K and reverse-biasing the detector from 0V to -0.5 V, applying the same voltage to all the pixels.

When the FPA is illuminated, $G_{\text{opt}}(\lambda_n)$ enters as a source term in the currents' continuity equations, providing the current under illumination $I_i(\lambda_n)$ collected by all the pixels

(the subscript i marks the i-th pixel). The same electrical problem was solved also in dark, obtaining the dark current $I_{i,\mathrm{dark}}$ (expected to be very similar for all the pixels).

The photocurrent follows as $I_{ph,i}(\lambda_n) = I_i(\lambda_n) - I_{i,\mathrm{dark}}$ and the quantum efficiency as

$$\mathrm{QE}_i(\lambda_n) = \frac{I_{ph,i}(\lambda_n)}{qN_{\mathrm{phot},i}(\lambda_n)}, \tag{2}$$

where q is the elementary charge and $N_{\mathrm{phot},i}$ is the photon flux impinging the i-th pixel's illuminated face. To this end, the detector in Fig. 1 was discretized into $\approx 0.95 \times 10^6$ elements with a meshing tool which generates a denser grid in regions where gradients of current density, electric field, free charge density and material composition are present.

Combined electromagnetic (optical) and electrical simulations allow to define a useful figure of merit, *i.e.* the ratio $\mathscr{C}_i$ between the photocurrent collected by the electrical contacts of the i-th pixel and of the CP,

$$\mathscr{C}_i(\lambda_n) = \frac{I_{ph,i}(\lambda_n)}{I_{ph,\mathrm{CP}}(\lambda_n)}, \tag{3}$$

that can be regarded as a possible definition of the *total* inter-pixel crosstalk. Considering in particular the NNs, $\mathscr{C}_{\mathrm{NNs}}(\lambda_n)$ depends *a*) on carriers photogenerated in the CP diffusing to the neighboring ones (yielding a *diffusive* crosstalk, $\mathscr{D}_{\mathrm{NNs}}(\lambda_n)$), and *b*) on carriers directly photogenerated in the NNs by the illuminating Gaussian beam tail [22] (*optical* crosstalk). The latter can be defined as the ratio between carriers photogenerated in one of the NNs (with volume V_{NNs}) and those photogenerated in the CP (with volume V_{CP})

$$\mathscr{O}_{\mathrm{NNs}}(\lambda_n) = \frac{\int_{V_{\mathrm{NNs}}} G_{\mathrm{opt}}(x,y,z;\lambda_n)\,dx\,dy\,dz}{\int_{V_{\mathrm{CP}}} G_{\mathrm{opt}}(x,y,z;\lambda_n)\,dx\,dy\,dz}, \tag{4}$$

whereas the separation of *diffusive* crosstalk can be obtained following the approach described in our previous work [23]. In short, first we defined the *diffusive* crosstalk as the ratio $\mathscr{D}_{\mathrm{NNs}} = I_{\mathrm{diff,NNs}}/I_{ph,\mathrm{CP}}$, where $I_{\mathrm{diff,NNs}}$ is the contribution to $I_{ph,\mathrm{NNs}}$ coming from carriers photogenerated in the CP and diffused to the NNs (in order to simplify the notation, the λ_n-dependence is implicit). The other contribution to $I_{ph,\mathrm{NNs}}$ is the current $I_{\mathrm{tail,NNs}}$, coming from carriers really photogenerated in the NNs themselves by the beam tail, proportional to $\int_{V_{\mathrm{NNs}}} G_{\mathrm{opt}}(x,y,z)\,dx\,dy\,dz$, hence proportional to $\mathscr{O}_{\mathrm{NNs}}$. At least as a first approximation, we obtained from (3) and (4)

$$\mathscr{D}_{\mathrm{NNs}} = \mathscr{C}_{\mathrm{NNs}} - \frac{I_{\mathrm{tail,NNs}}}{I_{ph,\mathrm{CP}}} \approx \mathscr{C}_{\mathrm{NNs}} - \mathscr{O}_{\mathrm{NNs}}, \tag{5}$$

having exploited the proportionality between the photocurrent and the integral of G_{opt} over the pixel volume appearing in the definition of $\mathscr{O}_{\mathrm{NNs}}$. The expected minority carrier (hole) diffusion length $L_d = \sqrt{\mu_p \tau_p k_B T/q}$ in the absorber depends on the hole mobility μ_p and lifetime $\tau_p = (\tau_{\mathrm{Auger}}^{-1} + \tau_{\mathrm{SRH}}^{-1})^{-1}$, where q and k_B are the elementary charge and the Boltzmann's constant. L_d cannot be given a unique value at a given temperature, since it depends on the carrier density and energy gap, which are both point-dependent because of the applied bias and the absorber compositional grading. Just to have an estimate, we chose an intermediate composition $x = 0.23$, evaluating n, p and n_i at equilibrium, keeping into account the incomplete dopant ionization and Fermi statistics as described in Section 2. Expressing μ_p and Auger coefficients according to [22, Table I], and τ_{Auger} according to [48, Eq. 3.4], one

has $\tau \approx 15\,\mu$s and $L_d \approx 81\,\mu$m at $T = 140$ K, in substantial agreement with numerical results in [24,25,48,49]. This result reinforces and justifies the need for obtaining satisfactory carrier depletion in the absorber, in order to make photogenerated carriers to drift efficiently towards the electrical contact before they diffuse.

4 Results and discussion

All simulations were obtained considering Auger and SRH as generation-recombination (GR) processes, neglecting instead radiative processes. Extensive discussion about this important point can be found in [50] and references therein. At the moderate reverse bias considered in the present work (not higher than -0.5 V), the band-to-band, trap-assisted tunneling and impact ionization may be safely neglected [28–30]. Section 4.1 refers to a set of simulations in dark, showing the connection between carrier depletion, Auger suppression and dark current. This is a well known concept, but a discussion is useful to illustrate the central scope of this work: the connection between carrier depletion and inter-pixel crosstalk, addressed in the Section 4.2.

4.1 Carrier depletion, Auger suppression and dark current

In Fig. 2(a,b) band diagrams along a vertical cutline at the miniarray's center are shown for $V_{\rm bias} = -0.1$ V and $V_{\rm bias} = -0.5$ V, when $T = 140$ K. In Fig. 2(c) the electron, hole, and intrinsic densities n, p and n_i are shown in dark for the same values of T and $V_{\rm bias}$.

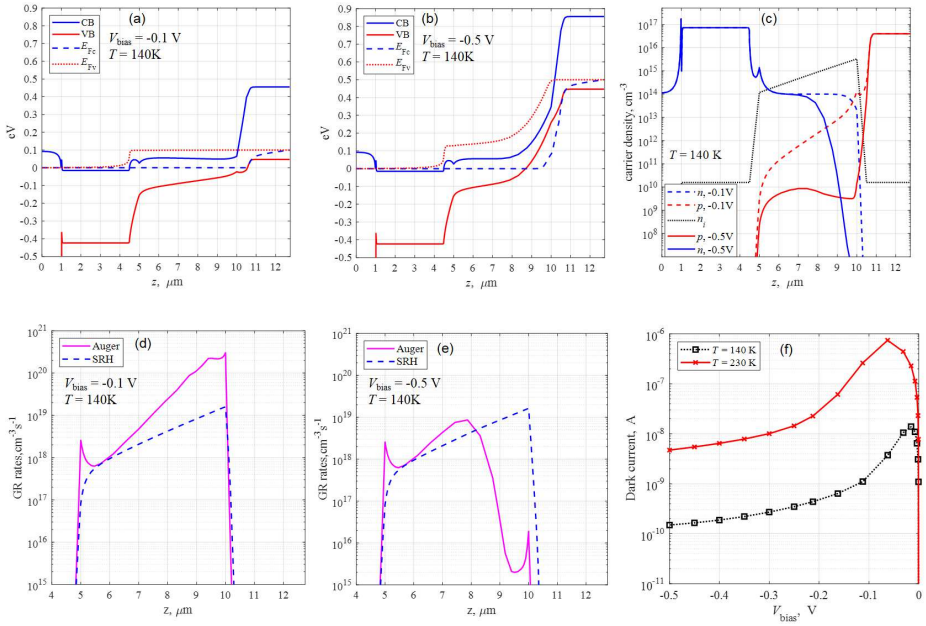

Fig. 2 For $V_{\rm bias} = -0.1$ V and -0.5 V, temperature $T = 140$ K, the figure shows: (a,b) band diagrams (along a vertical cutline at the miniarray's center); (c) electron (n), hole (p), and intrinsic (n_i) densities; (d,e) Auger and SRH generation rates. In panel (f) the dark current, for $T = 140$ K and $T = 230$ K is reported.

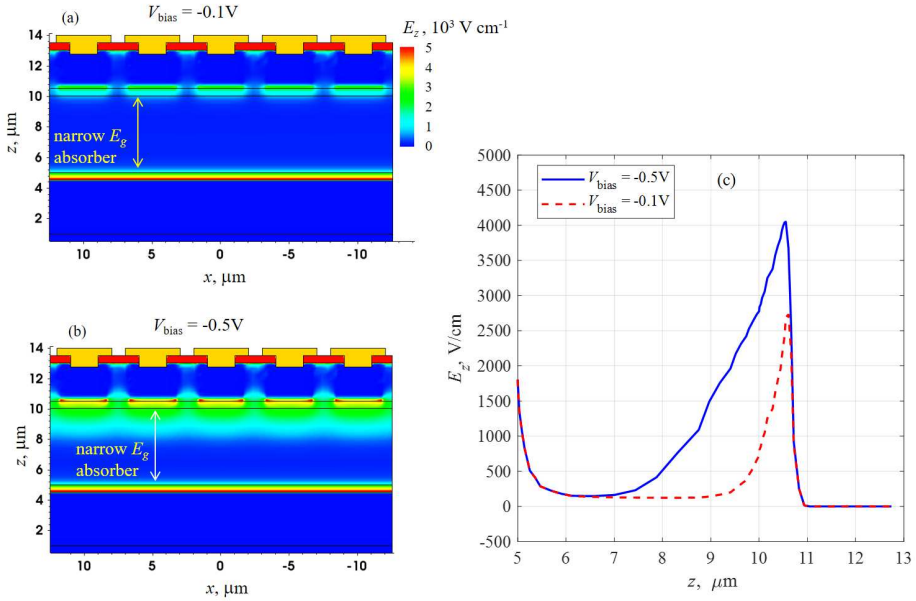

Fig. 3 Magnitude of the z-component of the electric field E_z in the miniarray, for $V_{\text{bias}} = -0.1$ V and -0.5 V (panels (a) and (b) respectively), at $T = 140$ K (the same color scale holds for both panels). E_z is also shown in panel (c) along a vertical 1D cutline at $x = 0$.

The effect of carrier depletion is well visible: even at $V_{\text{bias}} = -0.1$ V, n and p in the absorber ($5\,\mu\text{m} \leq z \leq 10\,\mu\text{m}$) are below the intrinsic density (dashed lines), and as soon as the reverse bias increases to -0.5 V, their values drop to very low values (solid lines), especially in the upper part of the absorber. A consequence of this behavior is the suppression of the Auger generation, as visible in Fig. 2(d,e), increasingly effective with increasing reverse bias. This fact makes the simulated dark current I_{dark} to *decrease* progressively and considerably with increasing V_{bias} (after a maximum value is reached around -0.05 V), as shown in Fig. 2(f), confirming a behavior obtained by other groups [3, 25] for similar carrier-depleted absorbers. Even if the temperature is increased to $T = 230$ K, this behavior is still at play, as it is shown in the same plot (the plotted I_{dark} was obtained averaging $I_{i,\text{dark}}$ on all the pixels, excluding the outer ring, although the dark current resulted very similar for all them).

4.2 Carrier depletion and inter-pixel crosstalk

As long as reverse bias increases from -0.1 V to -0.5 V, carrier depletion in the absorber increases significantly, allowing a larger fraction of photogenerated carriers to drift towards the CP contact, before they diffuse laterally. This is what can be expected considering the distribution of the magnitude of the electric field in the miniarray, shown in Fig. 3(a,b) for $V_{\text{bias}} = -0.1$ V and -0.5 V respectively, at $T = 140$ K. For the higher reverse bias, carrier depletion causes a considerably larger space charge region in the absorber, where the electric field is above 10^3 V/cm approximately for half the absorber thickness.

The effect of carrier depletion on the efficiency of photogenerated carrier collection is apparent comparing the dashed and solid lines in Fig. 4(a), that shows QE_{CP} to increase

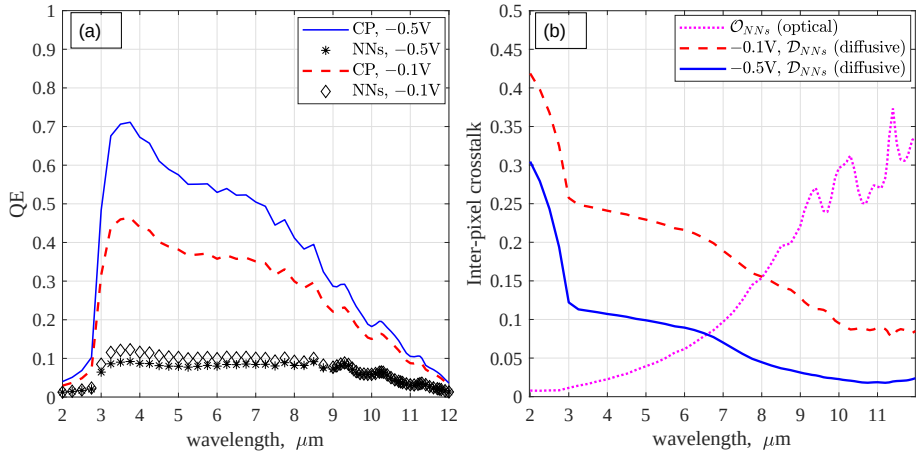

Fig. 4 (a) The CP and NNs spectral QE for the described Gaussian beam illumination centered on the CP, for $T = 140\,\mathrm{K}$ and $V_{\mathrm{bias}} = -0.1\,\mathrm{V}$ and $-0.5\,\mathrm{V}$. The λ sampling is finer for $\lambda > 9\,\mu\mathrm{m}$, since internal reflections and interference effects may generate a rich resonance-like phenomenology around the cutoff. (b) For the same temperature, the "optical" and "diffusive" inter-pixel crosstalk (adimensional ratios) are shown for $V_{\mathrm{bias}} = -0.1\,\mathrm{V}$ and $-0.5\,\mathrm{V}$ (the optical crosstalk is bias-independent).

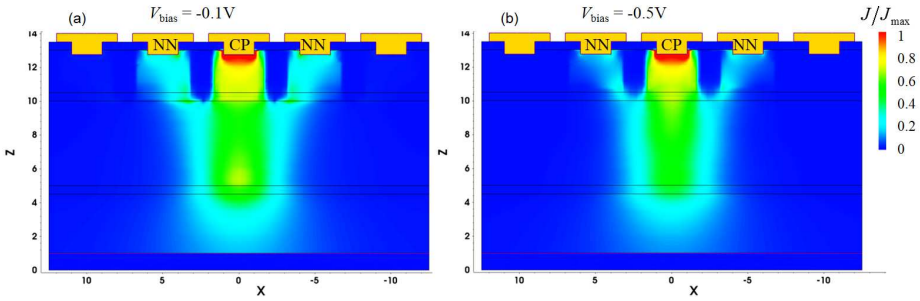

Fig. 5 Current density distribution for $V_{\mathrm{bias}} = -0.1\,\mathrm{V}$ and $-0.5\,\mathrm{V}$ (respectively, panels (a) and (b)), at $T = 140\,\mathrm{K}$, considering an illuminating Gaussian beam with $\lambda_n = 6\,\mu\mathrm{m}$ centered on the CP. In both panels, the current density has been normalized to its maximum value.

significantly when raising the reverse bias. However, if we only consider $\mathrm{QE}_{\mathrm{CP,NNs}}$ for the two bias points as shown in Fig. 4(a), it is not straightforward to understand how its behavior is related to inter-pixel crosstalk. Instead, a plot of $\mathscr{D}_{\mathrm{NNs}}$, obtained as outlined in Section 3.2 and shown in Fig. 4(b), makes the crosstalk information much more evident. The moderate electric field in the absorber that originates from the depletion of majority carriers is enough to curtail the inter-pixel "diffusive" crosstalk even at moderate reverse bias. Beside Auger suppression [3], this is an additional advantage of carrier-depleted detectors, that concur to include them among key components for high performing IR detectors.

A major feature is the significant decrease of diffusive crosstalk for increasing wavelength. This is due to the absorber compositional grading which decreases the energy gap at the top surface of the detector. Hence, most of LWIR radiation is absorbed there, where bias contacts are located. This favors carrier collection by the CP and decreases the value of $\mathscr{D}_{\mathrm{NNs}}$ for increasing λ.

The increase of carrier collection efficiency and the ensuing reduction of diffusive inter-pixel crosstalk can be qualitatively visualized in Fig. 5, where the current density distribution J, normalized to its maximum value, is shown along a vertical cutplane at miniarray's center, for $V_{\rm bias} = -0.1\,{\rm V}$ and $-0.5\,{\rm V}$ (respectively, left and right panel), at $T = 140\,{\rm K}$, having consideres – just as an example – an illuminating Gaussian beam with $\lambda_n = 6\,\mu{\rm m}$ centered on the CP. The diffusion current from the miniarray's axis towards the NNs results substantially decreased for the highest reverse bias, thanks to the increased magnitude of the electric field.

5 Conclusions

A known and effective strategy to decrease the Auger generation in the HgCdTe absorber, hence the dark current, consists in reducing the extension of the absorber quasi-neutral regions by majority carriers depletion. Employing three-dimensional, realistic full-wave electromagnetic and electrical simulations, we have shown that the same strategy is also effective in reducing the diffusive inter-pixel crosstalk, particularly important in planar detectors when the pixel size is much smaller than diffusion length. In particular, we considered a HgCdTe-based IR-FPA with pixel size of $5\,\mu{\rm m}$, with appropriate doping and composition profiles. Carrier depletion of the HgCdTe absorber is shown to cut down the diffusive inter-pixel crosstalk by more than a factor of two by increasing the reverse bias from $-0.1\,{\rm V}$ to $-0.5\,{\rm V}$. For $V_{\rm bias} = -0.5\,{\rm V}$, the value of $\mathscr{D}_{\rm NNs}$ appears to be limited between 2% and 5% in the LWIR band, and below 12% in the MWIR band. The most favorable value is for LWIR, since the narrowest value of bandgap is located closer to the upper part of the detector, where the magnitude of the electric field is higher, according to Fig. 3.

References

1. M.A. Kinch, J. Electron. Mater. **44**(9), 2969 (2015). DOI 10.1007/s11664-015-3717-5
2. M.A. Kinch, J. Electron. Mater. **29**(6), 809 (2000). DOI 10.1007/s11664-000-0229-7
3. J. Schuster, R.E. DeWames, P.S. Wijewarnasurya, J. Electron. Mater. **46**(11), 6295 (2017). DOI 10.1007/s11664-017-5736-x
4. T. Ashley, C.T. Elliott, Electron. Lett. **21**(10), 451 (1985). DOI 10.1049/el:19850321
5. C.T. Elliott, Semiconductor Sci. Tech. **5**(35), S30 (1990). DOI 10.1088/0268-1242/5/3S/008
6. P. Martyniuk, A. Rogalski, Opto-Electron. Rev. **21**(2), 239 (2013). DOI 10.2478/s11772-013-0090-x
7. S. Maimon, G.W. Wicks, Appl. Phys. Lett. **89**(15), 151109 (2006). DOI 10.1063/1.2360235
8. A.M. Itsuno, J.D. Phillips, S. Velicu, IEEE Trans. Electron Devices **58**(2), 501 (2011). DOI 10.1109/TED.2010.2093577
9. A.M. Itsuno, J.D. Phillips, S. Velicu, Appl. Phys. Lett. **100**(16), 161102 (2012). DOI 10.1063/1.4704359
10. J. Schuster, W.E. Tennant, E. Bellotti, P.S. Wijewarnasuriya, in Infrared Technology and Applications XLII, vol. 9819, Proceedings of the SPIE (2016), vol. 9819, Proceedings of the SPIE, p. 98191F. DOI 10.1117/12.2224383
11. W. Lei, J. Antoszewski, L. Faraone, Appl. Phys. Rev. **2**(4), 041303 (2015). DOI 10.1063/1.4936577
12. P. Martyniuk, W. Gawron, J. Pawluczyk, A. Keblowski, P. Madejezyk, A. Rogalski, J. Infrared Millim. Waves **34**, 385 (2015). DOI 10.11972/j.issn.1001-9014.2015.04.001
13. W.E. Tennant, D. Lee, M. Zandian, E. Piquette, M. Carmody, J. Electron. Mater. **37**(9), 1406 (2008). DOI 10.1007/s11664-008-0426-3
14. A. Rogalski, J. Antoszewski, L. Faraone, J. Appl. Phys. **105**(9), 091101 (2009). DOI 10.1063/1.3099572
15. C.A. Keasler, E. Bellotti, Appl. Phys. Lett. **99**(9), 091109 (2011). DOI 10.1063/1.3632110
16. J. Schuster, B. Pinkie, S. Tobin, C. Keasler, D. D'Orsogna, E. Bellotti, IEEE J. Select. Topics Quantum Electron. **19**(5), 800415 (2013). DOI 10.1109/JSTQE.2013.2256340
17. P. Martyniuk, J. Antoszewski, M. Martyniuk, L. Faraone, A. Rogalski, Appl. Phys. Rev. **1**, 041102 (2014). DOI 10.1063/1.4896193
18. O. Gravrand, J. Rothman, C. Cervera, N. Baier, C. Lobre, J.P. Zanatta, O. Boulade, V. Moreau, B. Fieque, J. Electron. Mater. **45**(9), 4532 (2016). DOI 10.1007/s11664-016-4516-3

19. A. Rogalski, P. Martyniuk, M. Kopytko, Rep. Prog. Phys. **79**(4), 046501 (2016). DOI 10.1088/0034-4885/79/4/046501
20. G.C. Holst, R.G. Driggers, Opt. Eng. **51**(9), 096401 (2012). DOI 10.1117/1.OE.51.9.096401
21. R.G. Driggers, R. Vollmerhausen, J.P. Reynolds, J. Fanning, G.C. Holst, Opt. Eng. **51**(6), 063202 (2012). DOI 10.1117/1.OE.51.6.063202
22. M. Vallone, M. Goano, F. Bertazzi, G. Ghione, W. Schirmacher, S. Hanna, H. Figgemeier, J. Electron. Mater. **46**(9), 5458 (2017). DOI 10.1007/s11664-017-5378-z
23. M. Vallone, M. Goano, F. Bertazzi, G. Ghione, S. Hanna, D. Eich, H. Figgemeier, IEEE J. Electron Devices Soc. **6**(1), 664 (2018). DOI 10.1109/JEDS.2018.2835818
24. J. Wenus, J. Rutkowski, A. Rogalski, IEEE Trans. Electron Devices **48**(7), 1326 (2001). DOI 10.1109/16.930647
25. A. Rogalski, M. Kopytko, P. Martyniuk, Appl. Opt. **57**(18), D11 (2018). DOI 10.1364/AO.57.000D11
26. H. Kroemer, Rev. Modern Phys. **73**(3), 783 (2001). DOI 10.1103/RevModPhys.73.783
27. M. Calciati, A. Tibaldi, F. Bertazzi, M. Goano, P. Debernardi, Semiconductor Sci. Tech. **32**(5), 055007 (2017). DOI 10.1088/1361-6641/aa66bb
28. M. Vallone, M. Mandurrino, M. Goano, F. Bertazzi, G. Ghione, W. Schirmacher, S. Hanna, H. Figgemeier, J. Electron. Mater. **44**(9), 3056 (2015). DOI 10.1007/s11664-015-3767-8
29. M. Mandurrino, G. Verzellesi, M. Goano, M. Vallone, F. Bertazzi, G. Ghione, M. Meneghini, G. Meneghesso, E. Zanoni, in 14th International Conference on Numerical Simulation of Optoelectronic Devices (NUSOD 2014) (Palma de Mallorca, Spain, 2014), pp. 13–14. DOI 10.1109/NUSOD.2014.6935332
30. M. Mandurrino, M. Goano, M. Vallone, F. Bertazzi, G. Ghione, G. Verzellesi, M. Meneghini, G. Meneghesso, E. Zanoni, J. Comp. Electron. **14**(2), 444 (2015). DOI 10.1007/s10825-015-0675-3
31. M. Mandurrino, G. Verzellesi, M. Goano, M. Vallone, F. Bertazzi, G. Ghione, M. Meneghini, G. Meneghesso, E. Zanoni, Phys. Status Solidi A **212**(5), 947 (2015). DOI 10.1002/pssa.201431743
32. A. Rogalski, Infrared detectors, 2nd edn. (CRC Press, Boca Raton, FL, 2011)
33. P. Capper, J. Garland (eds.), Mercury Cadmium Telluride. Growth, Properties and Applications (John Wiley & Sons, Chichester, U.K., 2011)
34. Synopsys, Inc., Mountain View, CA, Sentaurus Device User Guide. Version N-2017.09 (2017)
35. M. Vallone, M. Goano, F. Bertazzi, G. Ghione, S. Hanna, D. Eich, H. Figgemeier, Infrared Phys. Tech. **97**, 203 (2019). DOI 10.1016/j.infrared.2018.12.041
36. B. Pinkie, E. Bellotti, J. Electron. Mater. **42**(11), 3080 (2013). DOI 10.1007/s11664-013-2647-3
37. J.P. Berenger, J. Comp. Phys. **114**(2), 185 (1994). DOI 10.1006/jcph.1994.1159
38. Synopsys, Inc., Mountain View, CA, Sentaurus Device Electromagnetic Wave Solver User Guide. Version N-2017.09 (2017)
39. D. Vasileska, S.M. Goodnick, G. Klimeck, Computational Electronics. Semiclassical and Quantum Device Modeling and Simulation (CRC Press, Boca Raton, FL, 2010)
40. K. Yee, IEEE Trans. Antennas Propagation **14**(3), 302 (1966). DOI 10.1109/TAP.1966.1138693
41. M. Born, E. Wolf, Principles of Optics. Electromagnetic Theory of Propagation, Interference and Diffraction of Light, 7th edn. (Cambridge University Press, Cambridge, U.K., 1999)
42. C. Keasler, E. Bellotti, J. Electron. Mater. **40**(8), 1795 (2011). DOI 10.1007/s11664-011-1644-7
43. J. Liang, W. Hu, Z. Ye, L. Liao, Z. Li, X. Chen, W. Lu, J. Appl. Phys. **115**(18), 184504 (2014). DOI 10.1063/1.4876227
44. O. Akın, H.V. Demir, Appl. Phys. Lett. **110**, 143106 (2017). DOI 10.1063/1.4979664
45. M. Vallone, M. Goano, F. Bertazzi, G. Ghione, W. Schirmacher, S. Hanna, H. Figgemeier, J. Electron. Mater. **45**(9), 4524 (2016). DOI 10.1007/s11664-016-4481-x
46. M. Vallone, A. Palmieri, M. Calciati, F. Bertazzi, F. Cappelluti, G. Ghione, M. Goano, M. Bahl, E. Heller, R. Scarmozzino, S. Hanna, D. Eich, H. Figgemeier, J. Electron. Mater. **47**(10), 5742 (2018). DOI 10.1007/s11664-018-6424-1
47. F. Bertazzi, M. Goano, G. Ghione, A. Tibaldi, P. Debernardi, E. Bellotti, in Handbook of Optoelectronic Device Modeling and Simulation, ed. by J. Piprek (CRC Press, Boca Raton, FL, 2017), chap. 2, pp. 35–80. DOI 10.1201/9781315152301-4
48. M.A. Kinch, State-of-the-Art Infrared Detector Technology (SPIE, Bellingham, WA, 2014). DOI 10.1108/eb010297
49. M.A. Kinch, F. Aqariden, D. Chandra, P.K. Liao, H.F. Schaake, H.D. Shih, J. Electron. Mater. **34**(6), 880 (2005). DOI 10.1007/s11664-005-0036-2
50. M. Kopytko, K. Jóźwikowski, P. Martyniuk, A. Rogalski, Infrared Phys. Tech. **97**, 38 (2019). DOI 10.1016/j.infrared.2018.12.015